Research Article | Vol. 32, No. 22 / 21 Oct 2024 / Optics Express 38023
Optics EXPRESS

Dual-channel asymmetric absorption-transmission properties based on plasma metastructures-photonic crystals

LEI LEI, BAO-FEI WAN, SI-YUAN LIAO, AND HAI-FENG ZHANG*

College of Electronic and Optical Engineering & College of Flexible Electronics (Future Technology), Nanjing University of Posts and Telecommunications, Nanjing 210023, China
*hanlor@163.com

Abstract: In this paper, a kind of plasma metastructures-photonic crystals (PMPC) structure is proposed to investigate the absorption and transmission properties of electromagnetic waves (EWs) incident from opposite directions. The results show that the PMPC can achieve a dual-channel asymmetric absorption-transmission (AAT) phenomenon. At an operating bandwidth (*OB*) of 2.15~2.85 GHz, EWs are absorbed in the forward incidence and transmitted in the backward case, and a relative bandwidth (*RB*) with forward absorption above 0.9 is 28.0%. On the contrary, at an *OB* of 7.07~7.67 GHz, EWs can be transmitted in the forward propagation and absorbed in the backward case with a *RB* of 8.1%. Moreover, the effects of parameters such as applied magnetic field, incident angle, and tilt angle on AAT performance are investigated separately. The proposed dual-channel tunable AAT will further extend the application of asymmetric devices in the fields of optical communication and optical transmission.

1. Introduction

In recent years, photonic crystals (PCs) have received increasing attention from industry and academia because of their wide applications in optoelectronics, communications, and biochemistry [1]. PCs are a novel composite material with a periodic arrangement of high and low dielectric constants [1,2]. Due to the periodicity of the photonic band structure, the propagation of light through them can exhibit a completely different behavior from that of a uniform dielectric material [3,4]. PCs were first discovered by Yablonovitch in 1987 [5]. Due to their unique ability to control the propagation of light, they have attracted significant interest in various research areas such as waveguides [6], filters [7], sensors [8], and ring resonators [9]. In general, PCs can be classified into one-, two-, and three-dimensional cases [10]. Although the applications of two- and three-dimensional PCs have been gradually verified, one-dimensional PCs are more attractive due to their simple structure and special optical properties. Metastructures developed from metamaterials [11] have unique physical properties not typically found in natural materials, such as negative refractive index and negative dielectric constant [12]. Through the specific design of metastructures, it is possible to regulate the propagation direction and amplitude of electromagnetic waves (EWs), which is conducive to the integration and miniaturization of optical devices [13]. Metastructures-photonic crystals are a new type of artificial electromagnetic material that combines metastructures with the concept of traditional PCs. They allow the design and adjustment of the shape, size, and arrangement of metastructures to regulate and optimize the properties of PCs, thereby achieving specific optical properties and applications.

Asymmetric propagation of EWs means that a certain polarized wave incident on opposite sides of a structure can be propagated in various ways, including absorption, reflection, transmission, etc [14]. This characteristic has aroused significant research interest because of its crucial role in optical systems for all-optical computation [15], information processing [16], and unilateral sensing [17]. At present, various approaches have been explored to achieve asymmetry [18–20],

#536915 https://doi.org/10.1364/OE.536915
Journal © 2024 Received 17 Jul 2024; revised 28 Sep 2024; accepted 28 Sep 2024; published 7 Oct 2024

Optics EXPRESS

where the role of breaking time and space symmetry in generating asymmetry has been extensively demonstrated. In addition, artificial composite structures such as metamaterials [21], dielectric gratings [22], and PCs [23] have been reported to enable asymmetric propagation. Bokhari *et al.* [24] proposed a method to enhance the angular induction and asymmetric propagation of EWs by introducing angular splitting in the crystal cell of a split-ring resonator. This design method could effectively enhance electromagnetic cross-coupling and was capable of achieving broadband asymmetry with a fractional bandwidth of 27.1% in the range of 14.8 GHz to 19.4 GHz. Liu *et al.* [22] proposed an asymmetric device with a double-edge composite grating structure. This asymmetry was achieved by enhancing the coupling between the incident EWs and the metal grating by patterning the silver bars on the outer surface. The results showed that the device could produce asymmetric propagation at the short wavelength of 627 nm and the long wavelength of 1238 nm with dual frequency points. Although numerous studies have been conducted on asymmetric devices, they primarily concentrate on a single frequency band or multiple discrete frequency points. Current research on asymmetric phenomena mainly emphasizes transmission and reflection, however, the advancement of absorption-transmission phenomena has progressed at a slower pace. In an ideal electronic warfare, it is hoped that the detection waves from the enemy will be absorbed to achieve the purpose of stealth, while our EWs can also be smoothly emitted to interfere with the enemy. Consequently, realizing asymmetric absorption-transmission across two channels is of paramount importance.

Plasma is a macroscopic ionized body that behaves electrically neutral [25], and the motion of charged particles inside it can be affected by electromagnetic fields [25]. Similarly, plasma can interact with electromagnetic fields to undergo energy transfer, exhibiting anisotropy [26], dissipation [27], and diffusion [28]. Since control of EWs propagation can be achieved by adjusting plasma parameters such as density and temperature [29], there have been numerous studies on introducing plasma into PCs [30–32]. Wan *et al.* [33] introduced plasma defects into one-dimensional PCs and proposed a sensor based on localized defect mode resonance, which enabled the measurement of multiple physical quantities simultaneously. Almawgani *et al.* [34] investigated the tunable characteristics of a single-channel filter based on plasma-defected PCs. Numerous researchers have been studying the combination of plasma and PCs. However, most studies have focused on filters and sensors, and very few have applied them to asymmetric device design. Due to the excellent tunable properties of plasma, asymmetric EW tuning can be achieved [30]. This capability is highly significant in the fields of optical isolators, plasma antennas, and plasma stealth aircraft.

In this paper, a kind of plasma metastructures-photonic crystals (PMPC) structure is proposed to investigate the propagation properties of EWs incident from opposite directions. Due to asymmetry in plasma spatial structure distribution and the magneto-optical effect of light, the propagation properties of EWs exhibit significant differences when incident from the forward or backward direction in various wavelength bands. At an operating bandwidth (*OB*) of 2.15~2.85 GHz, EWs achieve forward absorption and backward transmission with a relative bandwidth (*RB*) of 28.0%. At an *OB* of 7.07~7.67 GHz, propagation characteristics change to forward transmission and backward absorption with a *RB* of 8.1%. The position of the absorption peak and *RBs* can be effectively controlled by adjusting the external magnetic field. The forward and backward absorption peaks corresponding to the two channels, respectively, show a red-shift trend, and *RBs* decrease as the magnetic field increases. These findings provide exciting new opportunities for designing tunable asymmetric devices. This paper primarily focuses on theoretical research. The current findings are predominantly based on numerical simulations, while experimental preparation is not the main emphasis of this study.

Optics EXPRESS

2. Theoretical model and formulations

The schematic structure of the proposed PMPC is shown in Fig. 1, where the PMPC is infinitely extended in the y-direction. Two coordinate systems, (x, y, z) and (x', y', z') are defined in Fig. 1. Where the coordinate system (x', y', z') is obtained by rotating the coordinate system (x, y, z) around the y-axis by an angle φ clockwise. The background is air and the dielectric constants of the plasma layer and the porous silicon layer are denoted by ε_A and ε_B, respectively, where $\varepsilon_B = 1.3$ [35]. The plasma layer and the porous silicon layer are periodically aligned along the x'-direction, and their thicknesses are denoted by d_A and d_B, where $d_A = 0.4$ mm, $d_B = 1.0$ mm, and the length of the hypotenuse $l = 50$ mm. In Fig. 1(b), EWs are incident on the xoz plane at an angle θ. The direction of the magnetic field of the transverse magnetic (TM) wave is perpendicular to the plane of propagation, and the electric field is located in the xoz plane. The arrows in two different directions at the top and bottom indicate the forward and backward incidence of EWs. φ denotes the tilt angle of the PMPC concerning the z-axis, and θ denotes the incidence angle of the TM wave, with the following specific values: $\varphi = 40$ ° and $\theta = 50$ °. When the TM wave is incident, the magnetized plasma can be viewed as an anisotropic medium and the relative permittivity is described as [36,37]

$$\varepsilon_A = \frac{\varepsilon_1^2 - \varepsilon_2^2}{\varepsilon_1} \tag{1}$$

where

$$\varepsilon_1 = 1 - \frac{\omega_p^2(\omega + i\nu_c)}{\omega[(\omega + i\nu_c)^2 - \omega_c^2]} \tag{2}$$

$$\varepsilon_2 = -\frac{\omega_p^2\omega_c}{\omega[(\omega + i\nu_c)^2 - \omega_c^2]} \tag{3}$$

where, $\omega_c = (eB_0/m)$ is the plasma electron oscillation frequency, $\omega_p = (n_e\, e^2/m\varepsilon_0)^{1/2}$ is the plasma frequency, ω is the frequency of the incident EWs, ν_c is the collision frequency of electrons in the plasma, and m is the mass of the electron, e is the charge of the electron, n_e is the plasma density. In this paper, the relevant parameters are taken as follows: $B_0 = 0.1$ T, $n_e = 10^{18}\,\mathrm{m}^{-3}$, and $\nu_c = 0.1\omega_p$[37].

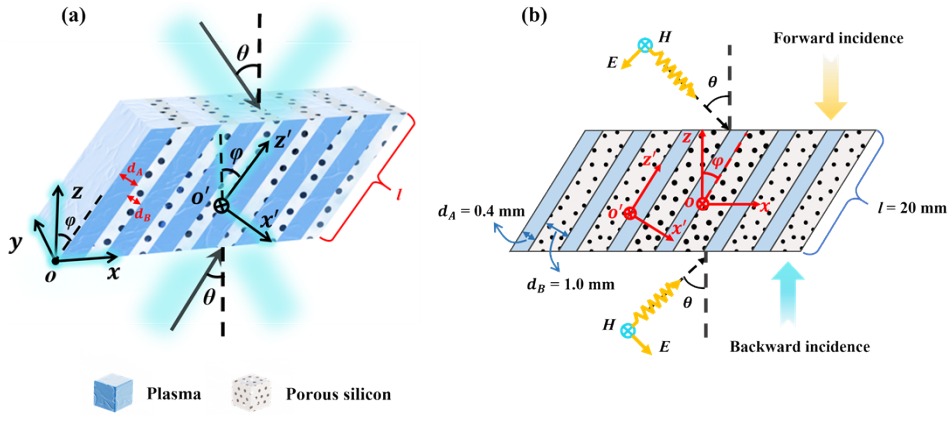

Fig. 1. (a) Structural three-dimensional view of the PMPC. (b) Side view of the PMPC and its dimensional parameters. The $x'y'z'$ axis is obtained by rotating the xyz axis about the y axis by an angle φ. The two opposing arrows at the top and bottom outside the PMPC indicate EWs incident in the forward and backward directions, respectively.

Optics EXPRESS

In the coordinate system $x'y'z'$, the effective relative permittivity tensor of the PMPC is [38]

$$\varepsilon' = \begin{bmatrix} \varepsilon_{xx}' & 0 & 0 \\ 0 & \varepsilon_{yy}' & 0 \\ 0 & 0 & \varepsilon_{zz}' \end{bmatrix} \tag{4}$$

Following the effective medium model [39], the PMPC can be described as uniaxial anisotropic media. The permittivity tensor component ε_{xx}', corresponding to polarization parallel to the axis (orthogonal to the layers) is positive, and the components ε_{yy}' and ε_{zz}' corresponding to polarization orthogonal to the axis (parallel to the layers) is negative. Formulas for effective parameters are as follows [39]

$$\frac{1}{\varepsilon_{xx}'} = \frac{1}{d_A + d_B}\left(\frac{d_A}{\varepsilon_A} + \frac{d_B}{\varepsilon_B}\right) \tag{5}$$

$$\varepsilon_{yy}' = \varepsilon_{zz}' = \frac{d_A\varepsilon_A + d_B\varepsilon_B}{d_A + d_B} \tag{6}$$

The relation between the coordinate system xyz and the coordinate system $x'y'z'$ is as follows [38]

$$\begin{bmatrix} x \\ y \\ z \end{bmatrix} = \begin{bmatrix} \cos\varphi & 0 & \sin\varphi \\ 0 & 1 & 0 \\ -\sin\varphi & 0 & \cos\varphi \end{bmatrix} \begin{bmatrix} x' \\ y' \\ z' \end{bmatrix} \tag{7}$$

In the coordinate system xyz, the effective relative permittivity tensor of the PMPC can be described as [38]

$$\varepsilon = \begin{bmatrix} \varepsilon_{xx} & 0 & \varepsilon_{xz} \\ 0 & \varepsilon_{yy} & 0 \\ \varepsilon_{zx} & 0 & \varepsilon_{zz} \end{bmatrix} \tag{8}$$

where, ε_{xx}, ε_{yy}, and ε_{zz} can be represented as

$$\varepsilon_{xx} = \varepsilon_{xx}'\cos^2\varphi + \varepsilon_{yy}'\sin^2\varphi \tag{9}$$

$$\varepsilon_{zz} = \varepsilon_{xx}'\sin^2\varphi + \varepsilon_{yy}'\cos^2\varphi \tag{10}$$

$$\varepsilon_{xz} = \varepsilon_{zx} = (\varepsilon_{yy}' - \varepsilon_{xx}')\sin\varphi\cos\varphi \tag{11}$$

The electric displaces vector $\mathbf{D'}$ and electric filed vector $\mathbf{E'}$ in the coordinate system $x'y'z'$ is [38]

$$\mathbf{D}' = \varepsilon_0\varepsilon'\mathbf{E}' \tag{12}$$

Similarly, in the coordinate system xyz, it is

$$\mathbf{D} = \varepsilon_0\varepsilon\mathbf{E} \tag{13}$$

Since the magnetic field has only y-directional components for both forward and reverse incidence of the TM waves, the magnetic field can be expressed as [38]

$$\mathbf{H}_y = H_y^+\vec{y} + H_y^-\vec{y} = H_{y0}^+ e^{i(k_{z+}\cdot z + k_x\cdot x - \omega t)}\vec{y} + H_{y0}^- e^{i(k_{z-}\cdot z + k_x\cdot x - \omega t)}\vec{y} \tag{14}$$

Optics EXPRESS

where k_{z+} and k_{z-} indicate the + z and -z components of wave vectors, respectively.

$$\nabla \times \mathbf{H}_y = \begin{vmatrix} \vec{x} & \vec{y} & \vec{z} \\ \frac{\partial}{\partial x} & \frac{\partial}{\partial y} & \frac{\partial}{\partial z} \\ 0 & H_y & 0 \end{vmatrix} = (-ik_{z+}H_y^+ - ik_{z-}H_y^-)\vec{x} + ik_x(H_y^+ + H_y^-)\vec{z} \tag{15}$$

Based on Eqs. (7) and (12), we can get [38]

$$\begin{bmatrix} D_x \\ 0 \\ D_z \end{bmatrix} = \varepsilon_0 \begin{bmatrix} \varepsilon_{xx} & 0 & \varepsilon_{xz} \\ 0 & \varepsilon_{yy} & 0 \\ \varepsilon_{zx} & 0 & \varepsilon_{zz} \end{bmatrix} \begin{bmatrix} E_x \\ 0 \\ E_z \end{bmatrix} \tag{16}$$

$$\frac{\partial \mathbf{D}}{\partial t} = -i\omega\varepsilon_0(\varepsilon_{xx}E_x + \varepsilon_{xz}E_z)\vec{x} - i\omega\varepsilon_0(\varepsilon_{zx}E_x + \varepsilon_{zz}E_z)\vec{z} \tag{17}$$

According to Maxwell's equations, we can derive [38]

$$\begin{aligned} k_{z+}H_y^+ + k_{z-}H_y^- &= \omega\varepsilon_0(\varepsilon_{xx}E_x + \varepsilon_{xz}E_z) \\ k_x(H_y^+ + H_y^-) &= -\omega\varepsilon_0(\varepsilon_{zx}E_x + \varepsilon_{zz}E_z) \end{aligned} \tag{18}$$

$$E_x = \frac{\varepsilon_{zz}k_{z+} + \varepsilon_{xz}k_x}{\omega\varepsilon_0(\varepsilon_{xx}\varepsilon_{zz} - {\varepsilon_{xz}}^2)}H_y^+ + \frac{\varepsilon_{zz}k_{z-} + \varepsilon_{xz}k_x}{\omega\varepsilon_0(\varepsilon_{xx}\varepsilon_{zz} - {\varepsilon_{xz}}^2)}H_y^- \tag{19}$$

for the + z direction plane wave, from $\nabla \times \mathbf{E} = -\frac{\partial \mathbf{B}}{\partial t}$, we can get [38]

$$\left(\frac{\partial \mathbf{E}_x}{\partial z} - \frac{\partial \mathbf{E}_z}{\partial x}\right) = i\omega\mu_0\mu H_y^+ \tag{20}$$

According to Eq. (18), the following results can be obtained

$$\varepsilon_{zz}{k_z}^2 + (\varepsilon_{xz}k_x + k_x\varepsilon_{zx})k_z + \varepsilon_{xx}{k_x}^2 = {k_0}^2(\varepsilon_{xx}\varepsilon_{zz} - {\varepsilon_{xz}}^2) \tag{21}$$

The two results of solving Eq. (21) are as follows

$$k_{z1} = \left[-\varepsilon_{xz}k_x + \sqrt{({\varepsilon_{xz}}^2 - \varepsilon_{zz}\varepsilon_{xx})({k_x}^2 - {k_0}^2\varepsilon_{zz})}\right] / \varepsilon_{zz} \tag{22}$$

$$k_{z2} = \left[-\varepsilon_{xz}k_x - \sqrt{({\varepsilon_{xz}}^2 - \varepsilon_{zz}\varepsilon_{xx})({k_x}^2 - {k_0}^2\varepsilon_{zz})}\right] / \varepsilon_{zz} \tag{23}$$

where, $k_x = k_0 \sin\theta, k_0 = \omega/c$ [38].

Eqs. (22) and (23) indicate that EWs are incident in two different directions, forward and backward, respectively. For ordinary materials, the values of k_{z1} and k_{z2} are inverses and can be viewed as invertible. However, in the PMPC, k_x is a constant that is not zero. As a result, EWs propagate differently at forward and backward incidence, which is the origin of the AAT property.

3. Analysis and discussion

To clearly explain the mechanism of the dual-band AAT of the PMPC, based on the parameters given above and Eqs. (22) and (23), the trends of the imaginary and real parts of the normal wave vector component k_z with respect to the operating frequency in opposite directions of EWs incidence are plotted in Fig. 2. First, the change in the imaginary part of k_z shown in

Optics EXPRESS

Fig. 2(a) illustrates the energy loss of electromagnetic waves propagating in the PMPC at different frequencies. The greater the absolute value of the imaginary part of k_z, the higher absorption rate of EWs. Conversely, when this value approaches zero, it indicates that transmission becomes easier. Specifically, k_{z1} attains a minimum (maximum absolute value) at $f = 2.8$ GHz, while k_{z2} reaches a maximum at $f = 7.2$ GHz. This indicates the presence of AAT near these two frequencies. The variation in the real part of k_z in Fig. 2(b) reflects changes in the propagation phase. The difference between the real part values of k_{z1} and k_{z2} indicates that the phase accumulation of the EWs differs between forward and backward incidence. Due to the asymmetry of the PMPC, EWs encounters distinct electromagnetic environments during forward and backward propagation, leading to differing phase accumulations. The primary reason for the observed asymmetry is that k_{z1} undergoes a mutation at approximately 7 GHz, transitioning from absorption to transmission. This mutation occurs due to ε_{zz} approaching zero at 7 GHz, as illustrated in Fig. 2(c). In conclusion, the results presented in Fig. 2 demonstrate that the PMPC can achieve dual-channel asymmetric propagation. This phenomenon arises from the differing responses of forward and backward incident EWs during propagation, which include variations in energy loss and phase change.

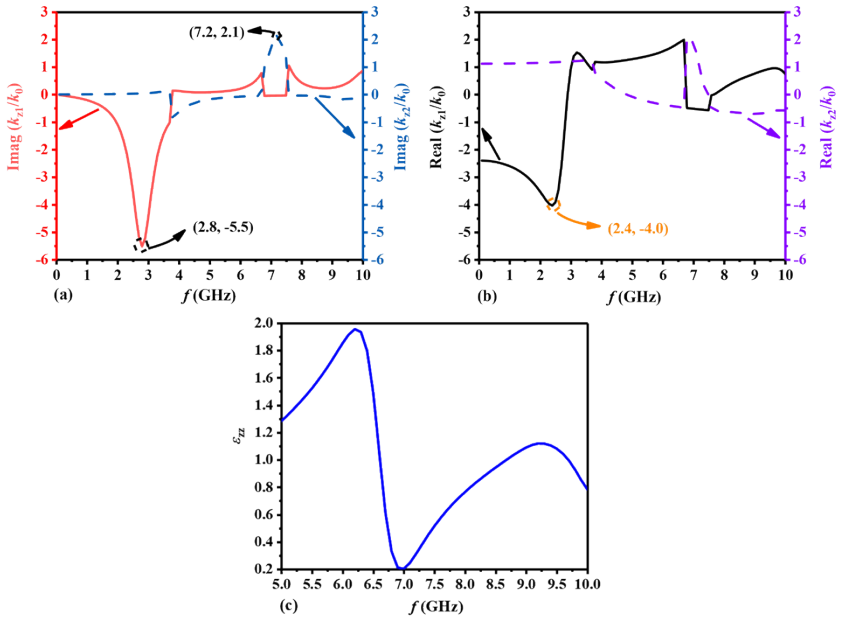

Fig. 2. (a) The imaginary parts and (b) the real parts of the two plane EWs in the PMPC. (c) The permittivity component ε_{zz}. k_{z1} represents the forward incidence of EWs, while k_{z2} denotes the backward incidence.

All simulation results presented in this paper were obtained using HFSS and calculated through the finite element method. During the simulation, the x-y plane was configured with periodic boundary conditions, while the z-direction was treated as open space. In the following results, the oblique incidence of EWs is a necessary condition.

As shown in Fig. 3, A denotes the absorptivity of the incident EWs and T denotes the transmittance. As the frequency increases, the AAT phenomenon appears in two different windows. In Fig. 3(a), when the TM wave is incident from the forward direction, the absorptivity reaches a maximum value of 1.0 at $f = 2.48$ GHz. For backward incidence, the transmittance is greater than 0.9 for an OB of 1.00~5.02 GHz. It is noteworthy that the forward absorptivity and backward transmittance are higher than 0.9 at OB of 2.15~2.85 GHz, exhibiting the AAT

Optics EXPRESS

phenomenon for incident waves, and the *RB* of absorptivity above 0.9 is 28.0%. In Fig. 3(b), propagation characteristics change, and the TM wave is mainly transmitted for forward incidence and absorbed for backward case. For forward incidence, the transmittance shows a tendency to decrease and then increase with the increase in frequency. When the *OB* is 6.56~8.28 GHz, the transmittance is greater than 0.9. For backward incidence, the absorptivity gradually increases with frequency and reaches a maximum value of 0.97 at $f = 7.43$ GHz. Similar to Fig. 3(a), the obvious AAT phenomenon is also exhibited at *OB* of 7.07~7.67 GHz, where the forward transmittance and backward absorptivity are both higher than 0.9, and *RB* is 8.1%. Comparing the two plots in Fig. 3, it can be concluded that the absorptivity and transmittance curves exhibit obvious dual-channel AAT characteristics when EWs are incident from opposite directions on the PMPC. This result is consistent with the variations of k_{z1} and k_{z2} in Fig. 2. Specifically, the imaginary part of k_{z1} reaches a minimum at $f = 2.8$ GHz and the imaginary part of k_{z2} reaches a maximum of $f = 7.2$ GHz, which corresponds to the fact that the PMPC exhibits asymmetry at *OBs* of 2.15~2.85 GHz and 7.07~7.67 GHz.

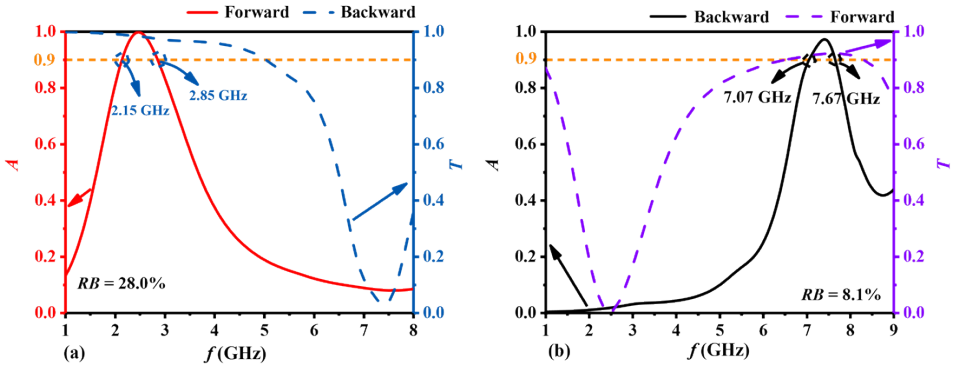

Fig. 3. (a) Forward absorptivity and backward transmittance curves of the PMPC. (b) Forward transmittance and backward absorptivity curves of the PMPC. The corresponding parameters are set as follows: $d_A = 0.4$ mm, $d_B = 1.0$ mm, $l = 50$ mm, $\varphi = 40°$, and $\theta = 50°$. For the plasma layer, the initial simulation conditions are $B_0 = 0.1$ T, $n_e = 10^{18}$ m^{-3}, and $\nu_c = 0.1\omega_p$. The *x*- and *y*-directions have periodic boundary conditions, while the *z*-direction is open space.

According to Eqs. (1) and (2), it is evident that the external magnetic field influences the electron oscillation frequency ω_c of the magnetized plasma, leading to a modification in its relative permittivity. This, in turn, impacts the absorptivity and transmittance curves. As demonstrated in Figs. 4(a)-(d), the impact of the magnetic field variation on the absorptivity and transmittance curves of PMPC is illustrated. In Fig. 4(a), when the TM wave is incident forward, the frequency corresponding to the peak absorptivity decreases with the increase of the magnetic field, showing a red-shift trend. When $B_0 = 0.3$ T, forward absorptivity reaches a maximum value of 1.0 at $f = 1.91$ GHz, and the *OB* with absorptivity above 0.9 is 1.69~2.09 GHz with *RB* of 21.2%. When $B_0 = 0.5$ T, forward absorptivity reaches a maximum value of 1.0 at $f = 1.41$ GHz, the *OB* is 1.30~1.53 GHz, and *RB* is 16.3%. As the value of the magnetic field continues to increase to 0.8 T and 1.0 T, the frequencies corresponding to the maximum value of the forward absorptivity shift to the right to $f = 0.98$ GHz and $f = 0.81$ GHz, and *RBs* decrease to 11.2% and 9.8%, respectively. In Fig. 4(b), when the TM wave is incident backward, the frequency corresponding to the peak of the backward absorptivity decreases with the increase of the magnetic field, showing a red-shift trend. Additionally, the *RB* also decreases. When $B_0 = 0.3$ T, the backward absorptivity reaches a maximum value of 0.94 at $f = 5.51$ GHz, the *OBs* with absorptivity above 0.9 range from 5.31 to 5.63 GHz, and the *RB* is 5.9%. When $B_0 = 0.5$

Optics EXPRESS

T, the backward absorptivity reaches a maximum value of 0.95 at $f = 4.20$ GHz, and the *OB* with absorptivity above 0.9 is 4.10~4.30 GHz with *RB* of 4.8%. As the value of the magnetic field continues to increase to 0.8 T and 1.0 T, the frequencies corresponding to the peaks of the backward absorptivity shift to the right to $f = 3.0$ GHz and $f = 2.5$ GHz, and the *RB* decreases to 3.0% and 2.4%, respectively. In Fig. 4(c), when the TM wave is incident in the forward direction, the PMPC exhibits high transmittance in the frequency range of 1.5~7.0 GHz. The transmittance curve demonstrates a red-shift trend with the increase of the magnetic field. In Fig. 4(d), when the TM wave is incident in the backward direction, the frequency corresponding to the lowest transmittance value exhibits the same red-shift trend. Moreover, when compared to Fig. 4(c), the minimum transmittance at backward incidence generally tends to increase under various magnetic fields. According to the analysis of Fig. 4, the PMPC is highly sensitive to changes in the magnetic field. An increase in the magnetic field results in a redshift of the absorptivity and transmittance curves. Simultaneously, the *RBs* corresponding to the forward and backward absorptivity decrease with the increase of the magnetic field.

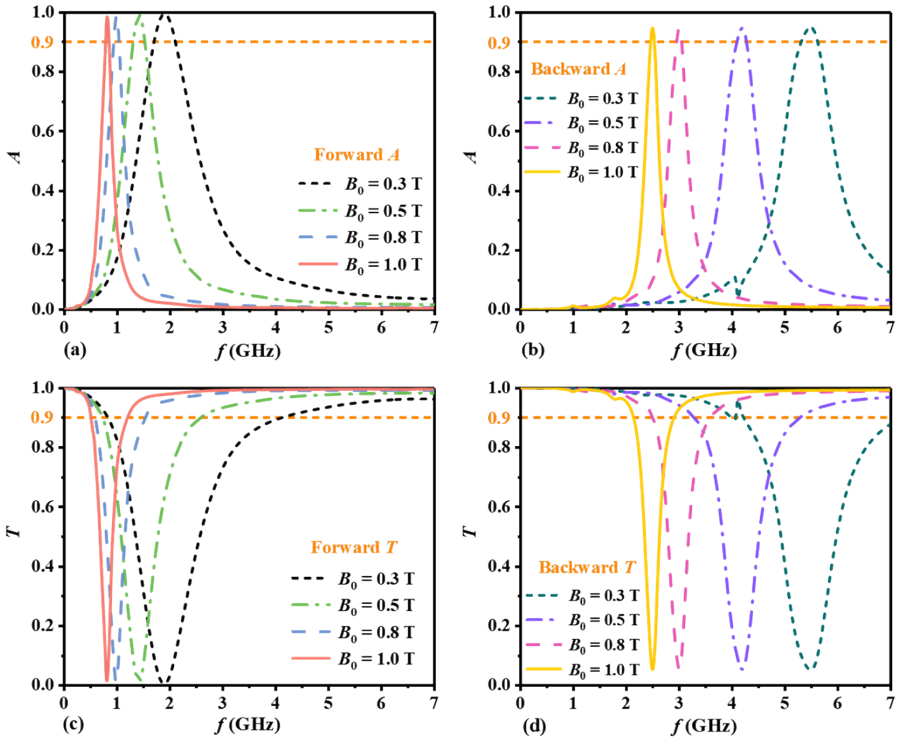

Fig. 4. Modulation of (a) forward absorptivity, (b) backward absorptivity, (c) forward transmittance, and (d) backward transmittance by magnetic fields.

To explain the phenomenon of absorption and transmission peak redshift illustrated in Fig. 4, we present the impact of magnetic field variation on the imaginary part of two normal wave vector components k_z incident from opposite directions in Fig. 5. The dielectric constant of plasma varies with changes in the external magnetic field, which in turn affects the equivalent refractive index of the PMPC and alters its propagation characteristics. In Fig. 5(a), when the incident wave is forward, the frequency corresponding to the minimum value of k_{z1} decreases as B_0 increases, indicating a redshift trend. The change in the imaginary part of k_z reflects the energy loss of EWs propagating in the PMPC, which corresponds to a change in the absorption curve. This explains the redshift of the forward absorption peak observed as the magnetic field

Optics EXPRESS

increases in Fig. 4(a). Similarly, Fig. 5(b) illustrates the redshift of the backward absorption peak shown in Fig. 4(b). Furthermore, since the peak value of the absolute value of k_{z1} is greater than that of k_{z2} under the same B_0, the forward absorption rate exceeds the backward absorption rate. This discrepancy accounts for the lower minimum value of forward transmission in Fig. 4(c) compared to the backward transmission in Fig. 4(d).

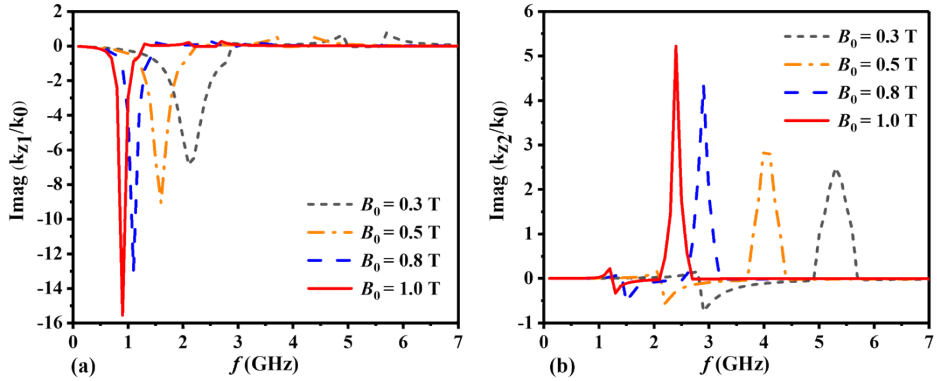

Fig. 5. The imaginary parts of the two plane EWs in the PMPC under varying external magnetic fields. (a) k_{z1} represents the forward incidence of EWs, while (b) k_{z2} denotes the backward incidence.

The spectra of forward absorptivity, backward absorptivity, forward transmittance and backward transmittance of the proposed PMPC with various incidence angles θ are illustrated in Fig. 6. In Fig. 6(a), with the TM wave incident in the forward direction, it can be seen that when the incident angle θ is in 5~20 °, the forward absorptivity is low. As θ increases, the forward absorptivity also increases gradually. The *OBs* with absorptivity greater than 0.8 are all located near 2 to 3 GHz. When $\theta = 50$ °, the forward absorptivity reaches its maximum value of 2.15~2.85 GHz, and the *RB* with a value higher than 0.9 is 28.0%. As θ continues to increase, the *OB* with absorptivity higher than 0.9 gradually decreases, while the *OB* with absorptivity higher than 0.8 continues to show an increasing trend. When $\theta = 72$ °, the absorptivity is below 0.8 at this point. In Fig. 6(b), when the TM wave is incident in the backward case, it is mainly absorbed at *OB* of 6.5~8 GHz. The absorptivity is low when the incident angle θ is small and shows an increasing trend as θ gradually increases. When $\theta = 50$ °, the absorption performance is the most excellent, and the *OB* of the backward absorptivity above 0.9 is 7.07~7.67 GHz and *RB* of 8.1%. When θ continues to increase, the absorptivity gradually decreases. At $\theta = 68$ °, the absorptivity is all lower than 0.9. When θ increases to 75 °, the absorptivity is all lower than 0.8, and the absorption performance gradually deteriorates. In Fig. 6(c), when the TM wave is incident in the forward direction, it is mainly transmitted in *OB* of 5~9 GHz. When the incidence angle θ is small, the frequency range with transmittance higher than 0.8 is divided into two parts, and the *OB* with transmittance higher than 0.9 is maximized as θ continues to increase to 40~50 °. In Fig. 6(d), when the backward incidence angle θ is small, the region of transmittance above 0.8 is divided into two parts. When θ is at 27 °~65 °, the region of transmittance higher than 0.8 is continuous, and the backward transmittance characteristic is most significant at $\theta = 50$ °, where the range of transmittance higher than 0.8 is the largest. According to the results in Fig. 6, better AAT performance of the dual-band can be obtained with θ at large incidence angles of 40 °~60 °, and blindly increasing θ does not enhance the AAT performance of the PMPC, which no longer exhibits excellent characteristics when θ exceeds 60 °. Therefore, selecting a suitable incidence angle is important for achieving excellent asymmetric characteristics. The interaction between EWs and PMPC is more complex due to the large angle of incidence. The oblique structure leads

Optics EXPRESS

to more intense scattering and phase changes at steep angles, resulting in asymmetric propagation of the two bands. This asymmetry arises from the selective response of PMPC to electromagnetic waves at varying angles, which is influenced by multiple physical mechanisms.

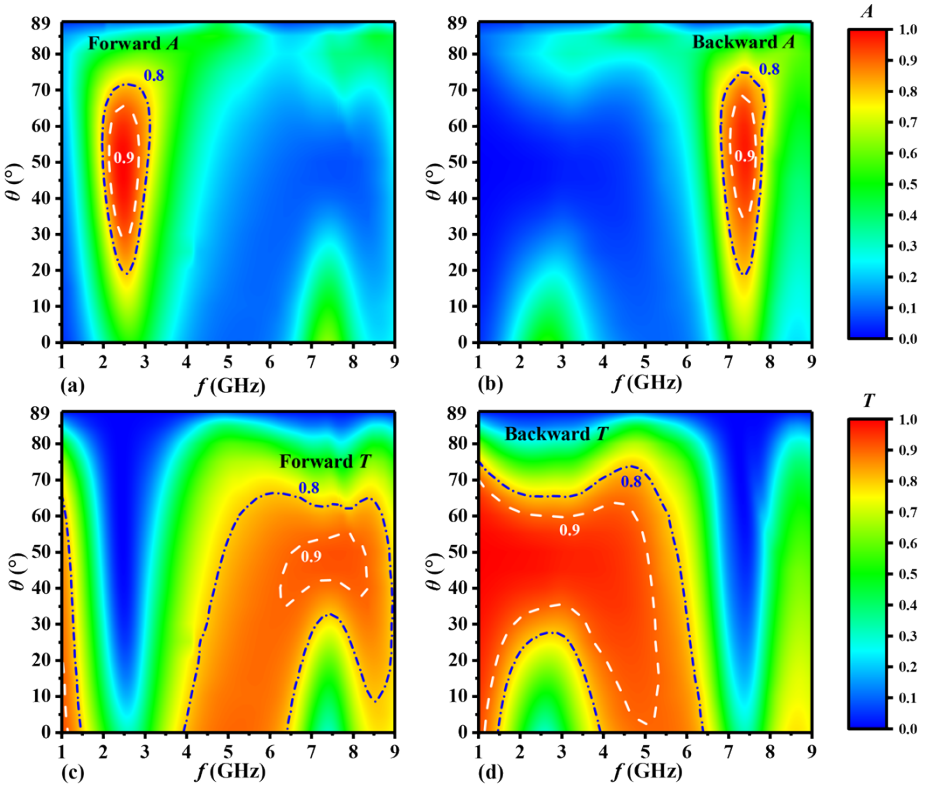

Fig. 6. (a) Forward absorptivity, (b) backward absorptivity, (c) forward transmittance, and (d) backward transmittance spectrum at different incidence angles θ.

As shown in Fig. 7(a), the frequency corresponding to the peak of the absorptivity curve gradually decreases with the increase of the tilt angle φ of the PMPC at the forward incidence of the TM wave, showing a trend of red-shift. In addition, the *RB* with an absorptivity higher than 0.9 exhibits a trend of first increasing and then decreasing with the gradual increase of φ. When $\varphi = 30$ °, the absorptivity curve has a peak at $f = 2.76$ GHz with a value of 0.96, and the *OB* with absorptivity higher than 0.9 is 2.48~3.13 GHz with *RB* of 23.2%. When the tilt angle φ is increased to 40 °, the absorptivity curve has a peak at $f = 2.48$ GHz of 1.0 with *OB* of 2.15~2.86 GHz, and *RB* of 28.3%. When $\varphi = 50$ °, the absorptivity curve continues to red-shift with a peak absorptivity of 0.95 at $f = 2.18$ GHz, *OB* of 1.95~2.44 GHz, and *RB* of 22.3%. Figure 7(b) shows that when the TM wave is incidence backward, the *RB* with absorptivity over 0.9 diminishes as φ increases. At $\varphi = 30$ °, 40 °, and 50 °, the *OBs* with absorptivity over 0.9 are 6.87~7.67 GHz, 7.07~7.67 GHz, and 7.26~7.43 GHz, equivalent to 11.0%, 8.1%, and 2.3% of *RBs*, respectively. In Fig. 7(c), when the TM wave is incident forward and the tilt angle φ is extended from 30 ° to 50 °, the forward transmittance curve is red-shifted, and the *RB* with transmittance above 0.9 grows and subsequently drops. At $\varphi = 30$ °, transmittance decreases as frequency increases, but at $\varphi = 40$ °, the transmittance increases at *OB* of 6.60~8.27 GHz, resulting in the *RB* of 22.5%. When φ continues to increase to 50 °, the *OB* is 6.36~7.31 and the *RB* is 13.9%. Figure 7(d) shows how the transmittance curves vary with increasing tilt angle

Optics EXPRESS

when EWs are incident backward. The *OBs* with transmittance greater than 0.9 are 1~2.77 GHz, 1~5.02 GHz, and 1~5.26 GHz at $\varphi = 30\,°$, 40 °, and 50 °, respectively. As the tilt angle increases, so do the *OBs*. Figure 7 shows that the tuning effect of the tilt angle φ on the absorptivity and transmittance curves is primarily reflected in the shifts of the *RBs* and the frequency at the peak of the absorption and transmittance. Specifically, as φ increases, the forward absorption and forward transmission curves become red-shifted. It is not difficult to explain that the primary reason for this phenomenon is that changing the inclination angle alters the effective dielectric constant of the PMPC, as can be seen from Eqs. (9)(10)(11). Based on the experience of Fig. 5, an increase in the inclination angle will result in a redshift of the peak in the imaginary part of k_z, which in turn will cause a redshift in the absorption and transmission curves.

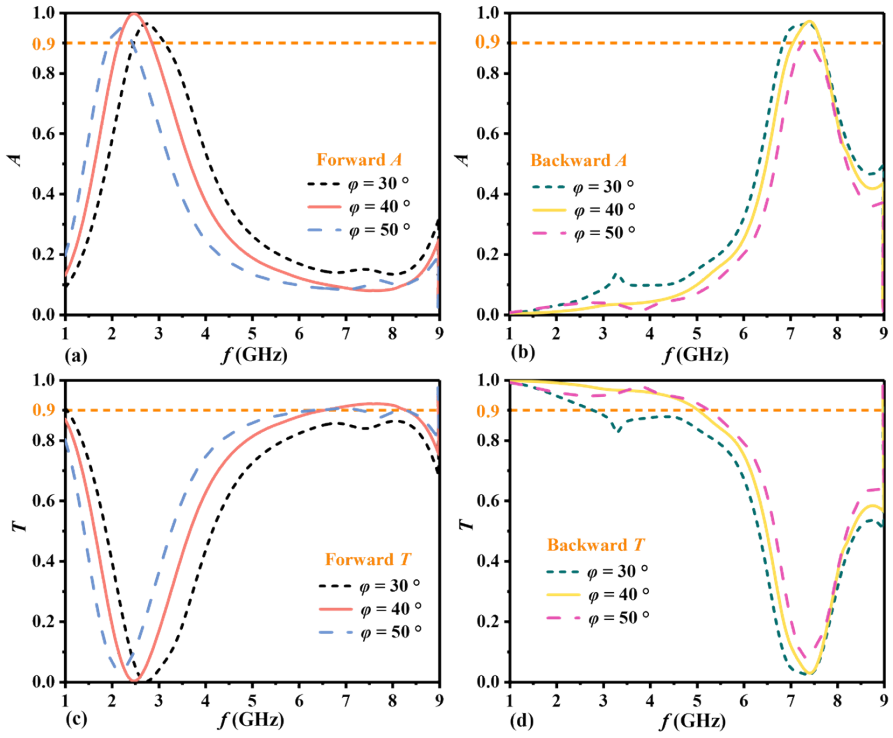

Fig. 7. Effects of different tilt angles φ ($\varphi = 30\,°$, 40 °, and 50 °) on (a) forward absorptivity, (b) backward absorptivity, (c) forward transmittance, and (d) backward transmittance curves.

As demonstrated in Fig. 8, the thickness of the plasma layer has a significant impact on the modification of EWs propagation properties. Figure 8(a) shows that when the TM wave is incident in the forward direction, the absorptivity curves blue-shift as d_A grows, and the *RB* with absorptivity greater than 0.9 progressively increases. At $d_A = 0.2$ mm, the *OB* with absorptivity above 0.9 is 1.75~1.98 GHz, whereas the *RB* is 12.3%. At $d_A = 1.0$ mm, the *OB* ranges from 2.69 to 3.98 GHz, whereas the *RB* is 38.7%. In Fig. 8(b), for the backward case, the *RB* of the backward absorptivity higher than 0.9 increases gradually when d_A increases, and absorptivity is all below 0.9 for $d_A = 0.2$ mm, and the *RB* is 18.7% for $d_A = 1.0$ mm. In Fig. 8(c), when the TM wave is incident forward, the transmittance curves exhibit a blue-shifted trend as d_A increases. Additionally, transmittance decreases with increasing d_A at high frequencies. When $f = 8.0$ GHz, the forward transmittance decreases from 0.95 to 0.72 as d_A increases from 0.2 mm to 1.0 mm. Figure 8(d) shows that when the TM wave is incident backward, the transmittance falls as d_A increases. When $d_A = 0.2$ mm, the *OB* with transmittance above 0.9 is 1.0~5.85 GHz. As d_A

Optics EXPRESS

increases to 1.0 mm, the *OB* with transmittance above 0.9 shifts to a lower frequency of 1~2.80 GHz. From Fig. 8, it can be seen that when EWs are incident forward, an increase in d_A results in a blueshift in both forward absorption and transmission, and also induces a change in *RBs*. When EWs are incident backward, an increase in d_A leads to a change in transmittance and absorption bandwidths.

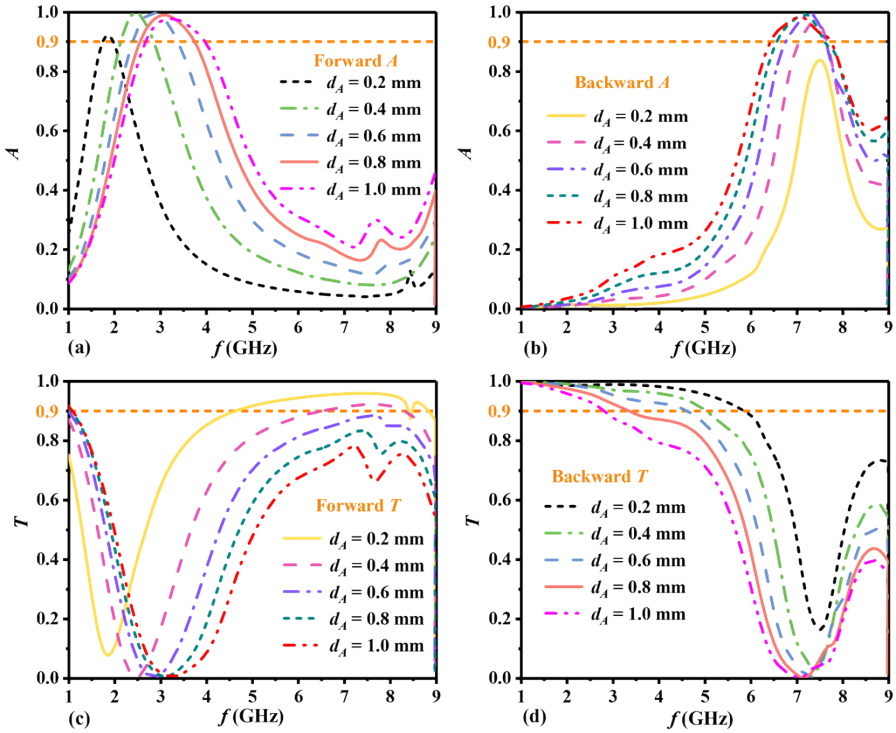

Fig. 8. Effects of the thickness d_A of the plasma layer on the (a) forward absorptivity, (b) backward absorptivity, (c) forward transmittance, and (d) backward transmittance curves.

The results presented in Fig. 8 indicate that variations in d_A significantly affect the absorption and transmission curves. Unlike previous observations, an increase in d_A leads to a greater redshift and an expanded bandwidth of the absorption curves. Based on the derivations of Eqs. (5)(6), it is evident that the thickness of the dielectric layer influences the effective dielectric constant and alters the wave vector components. This effect is illustrated in Fig. 9. As d_A increases, the virtual component of the forward incident wave, k_{z1}, shifts towards the blue, while the virtual component of the backward incident wave, k_{z2}, experiences an increase in bandwidth around 7 GHz. This observation demonstrates that the changes in the virtual component of k_z directly correspond to the variations in the absorption transmission curve depicted in Fig. 8.

The thickness d_B of the porous silicon layer affects the propagation properties of EWs, but not significantly, as Fig. 10 illustrates. When the TM wave is incident forward in Fig. 10(a), the absorptivity curves redshift as d_B increases, but *RBs* don't change much. The *OB* with absorptivity above 0.9 is 2.31~3.06 GHz and the *RB* is 27.4% when $d_B = 0.6$ mm. The *OB* is 2.01~2.67 GHz and the *RB* is 27.6% at $d_B = 1.4$ mm. In Fig. 10(b), it is evident that there are no discernible modulation effects of d_B on the backward absorptivity curves. In Fig. 10(c), transmittance curves exhibit a red-shift trend and an increase in transmittance as d_B increases when the TM wave is incident forward. The *OB* with transmittance above 0.9 runs from 6.03 to 8.58 GHz, with *RB* of 34.9%, as d_B rises to 1.4 mm. When the TM wave is incident backward, as

Optics EXPRESS

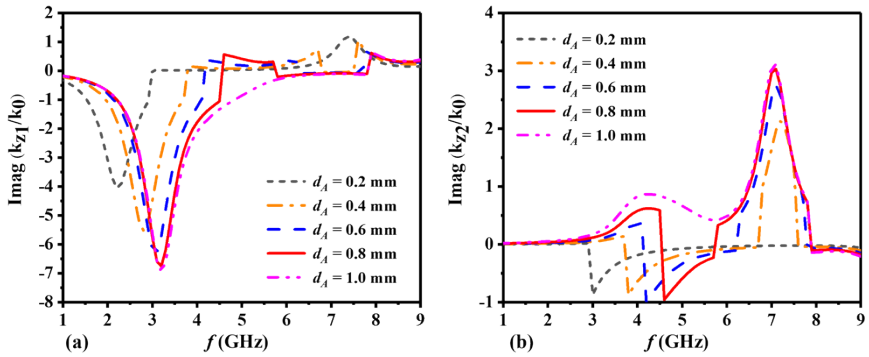

Fig. 9. The imaginary parts of the two plane EWs in the PMPC at different plasma thicknesses d_A. (a) k_{z1} represents the forward incidence of EWs, while (b) k_{z2} denotes the backward incidence.

shown in Fig. 10(d), the transmittance increases slightly with d_B, although this shift is not readily apparent.

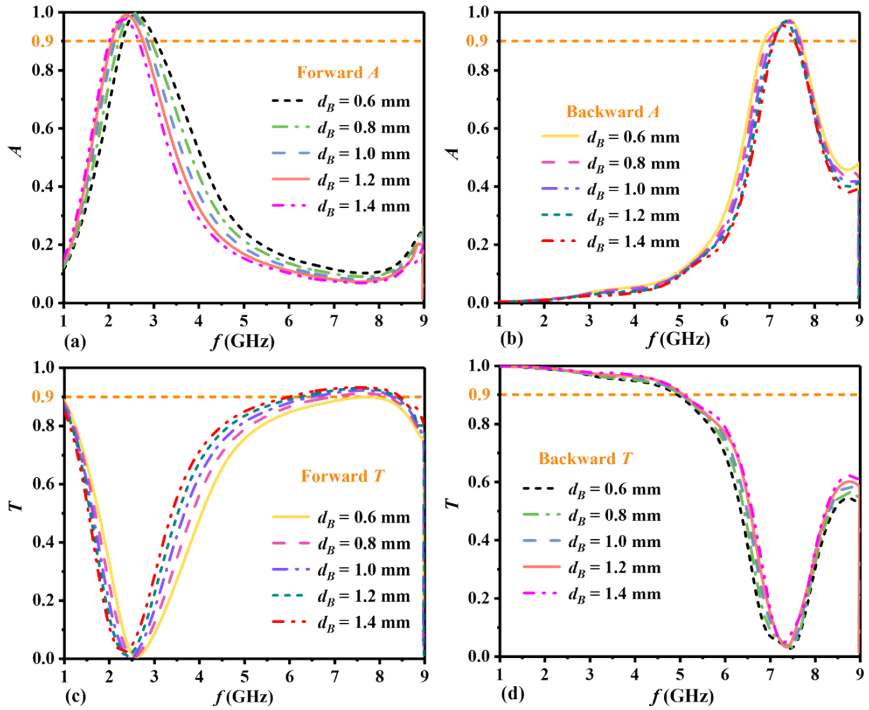

Fig. 10. Effects of the thickness d_B of the porous silicon layer on the (a) forward absorptivity, (b) backward absorptivity, (c) forward transmittance, and (d) backward transmittance curves.

To better understand the advantages of the designed PMPC compared to previously published reports, a specific performance analysis is presented in Table 1. Reference [22] demonstrates the asymmetry of dual-frequency points, Ref. [24] achieves tunable asymmetric transmission in open-ring resonators, Ref. [38] realizes asymmetric absorption using hyperbolic metamaterials, and Ref. [40] accomplishes ultra-wideband absorption. Unfortunately, all of these studies focused

Optics EXPRESS

on a single band or frequency point and only examined asymmetric absorption or asymmetric transmission. In contrast, the design proposed in this paper not only achieves high absorption in one direction and high transmission in the opposite direction across the dual frequency bands, but also allows for the adjustment of asymmetric characteristics through an external magnetic field. This capability holds significant value in the fields of radome technology and non-reciprocal isolators.

Table 1. Comparison of the asymmetric absorption-transmission of the PMPC with previous work

Refs.	Frequency range	Relative bandwidth	Frequency band	AAT	Tunable
[22]	627 nm	1% ($T > 0.6$)	Dual frequency points	None	None
	1238 nm	3% ($T > 0.6$)			
[24]	14.8~19.4 GHz	26.9% ($T > 0.9$)	Single band	None	Yes
[38]	1400~1600 nm	13.3% ($A > 0.9$)	Single band	None	None
[40]	5.7~13.1 GHz	78.1% ($A > 0.9$)	Single band	None	None
This work	2.15~2.85 GHz	28.0% ($A > 0.9$)	Dual bands	Yes	Yes
	7.07~7.67 GHz	8.1% ($A > 0.9$)			

4. Conclusion

In conclusion, the dual-band tunable AAT phenomena can be realized by the PMPC proposed in this paper. The TM wave is transmitted at the backward incidence and absorbed at the forward case with an *OB* of 2.15~2.85 GHz, and *RB* is 28.0%. With the *OB* of 7.07~7.67 GHz, the TM wave is transmitted at the forward incidence and absorbed at the backward case, and *RB* corresponding to a backward absorption above 0.9 is 8.1%. AAT is tuned by factors like tilt angle and magnetic field, and absorption and transmission curves are provided. According to the results, the tilt angle and magnetic field have a significant impact on the characteristics of the AAT generated by the PMPC. By adjusting the magnitude of the tilt angle and applying the magnetic field, it is possible to alter the *RBs* of the absorption and transmission curves as well as the frequency points that correspond to the peak. Furthermore, a detailed discussion of the mechanism for AAT characteristics is provided. The research in this paper can be applied to the design of multifunctional devices, nonreciprocal optical isolators, optical switches, optical absorbers, etc.

Funding. Postgraduate Research & Practice Innovation Program of Jiangsu Province (KYCX24_1160).

Disclosures. The authors declare no conflicts of interest.

Data availability. Data underlying the results presented in this paper are not publicly available at this time but may be obtained from the authors upon reasonable request.

References

1. J. D. Joannopoulos, P. R. Villeneuve, and S. Fan, "Photonic crystals," Solid State Commun. **102**(2-3), 165–173 (1997).
2. B. F. Wan, H. N. Ye, and H. F. Zhang, "Multi-channel angular selective window based on the epsilon-near-zero features of $YaBa_2Cu_3O_7$ material and photonic crystals ceramic structure of extremely small dispersion edge regions," Ceram. Int. **49**(22), 34814–34825 (2023).
3. K. Goodarzi and A. Mir, "Design and analysis of an all-optical demultiplexer based on photonic crystals," Infrared Phys. Technol. **68**, 193–196 (2015).
4. K. M. Ho, C. T. Chan, and C. M. Soukoulis, "Existence of a photonic gap in periodic dielectric structures," Phys. Rev. Lett. **65**(25), 3152–3155 (1990).
5. E. Yablonovitch, "Inhibited spontaneous emission in solid-state physics and electronics," Phys. Rev. Lett. **58**(20), 2059–2062 (1987).

Optics EXPRESS

6. L. Torrijos-Morán, A. Griol, and J. García-Rupérez, "Slow light bimodal interferometry in one-dimensional photonic crystal waveguides," Light: Sci. Appl. **10**(1), 16 (2021).
7. Y. Wang, D. Chen, G. Zhang, *et al.*, "A super narrow band filter based on silicon 2D photonic crystal resonator and reflectors," Opt. Commun. **363**, 13–20 (2016).
8. A. Bijalwan, B. K. Singh, and V. Rastogi, "Analysis of one-dimensional photonic crystal based sensor for detection of blood plasma and cancer cells," Optik **226**, 165994 (2021).
9. P. Andalib and N. Granpayeh, "All-optical ultracompact photonic crystal and gate based on nonlinear ring resonators," J. Opt. Soc. Am. B **26**(1), 10–16 (2009).
10. Y. Jia, P. Ren, and C. Fan, "Thermal tunable one-dimensional photonic crystals containing phase change material," Chin. Phys. B **29**(10), 104210 (2020).
11. R. H. Fan, B. Xiong, R. W. Peng, *et al.*, "Constructing metastructures with broadband electromagnetic functionality," Adv. Mater. (Weinheim, Ger.) **32**(27), 1904646 (2020).
12. H. R. Chen, Y. Z. Cheng, J. C. Zhao, *et al.*, "Multi-band terahertz chiral metasurface with giant optical activities and negative refractive index based on t-shaped resonators," Mod. Phys. Lett. B **32**(30), 1850366 (2018).
13. Y. Li, L. Zeng, H. Zhang, *et al.*, "Multifunctional and tunable metastructure based on VO_2 for polarization conversion and absorption," Opt. Express **30**(19), 34586–34600 (2022).
14. S. Li, L. R. Huang, Y. H. Ling, *et al.*, "High-performance asymmetric optical transmission based on coupled complementary subwavelength gratings," Sci. Rep. **9**(1), 17117 (2019).
15. D. Zhao, F. Fan, Z. Tan, *et al.*, "Tunable on-chip terahertz isolator based on nonreciprocal transverse edge spin state of asymmetric magneto-plasmonic waveguide," Laser Photonics Rev **17**(2), 2200509 (2023).
16. J. Han and R. Chen, "Dual-band metasurface for broadband asymmetric transmission with high efficiency," J. Appl. Phys. (Melville, NY, U. S.) **130**(3), 034503 (2021).
17. S. Cakmakyapan, H. Caglayan, A. E. Serebryannikov, *et al.*, "Experimental validation of strong directional selectivity in nonsymmetric metallic gratings with a subwavelength slit," Appl. Phys. Lett. **98**(5), 051103 (2011).
18. F. D. M. Haldane and S. Raghu, "Possible realization of directional optical waveguides in photonic crystals with broken time-reversal symmetry," Phys. Rev. Lett. **100**(1), 013904 (2008).
19. C. E. Rüter, K. G. Makris, R. El-Ganainy, *et al.*, "Observation of parity–time symmetry in optics," Nat. Phys. **6**(3), 192–195 (2010).
20. L. Feng, M. Ayache, J. Huang, *et al.*, "Nonreciprocal light propagation in a silicon photonic circuit," Science **333**(6043), 729–733 (2011).
21. F. Lv, L. Wang, Z. Xiao, *et al.*, "Asymmetric transmission polarization conversion of chiral metamaterials with controllable switches based on VO_2," Opt. Mater. (Amsterdam, Neth.) **114**, 110667 (2021).
22. H. Liu, Y. Zhang, C. Chen, *et al.*, "Dynamically adjustable and high-contrast asymmetric optical transmission based on bilateral compound metallic gratings," Opt. Laser Technol. **140**, 107033 (2021).
23. Y. Xu, B. Wan, Z. Zhou, *et al.*, "Tunable and asymmetric optical bistability of one-dimensional photonic crystals based on insb and nonlinear materials," Appl. Opt. **59**(31), 9799–9806 (2020).
24. S. H. A. Bokhari and H. M. Cheema, "Broadband asymmetric transmission via angle-induced chirality enhancement in split ring resonators," J. Appl. Phys. (Melville, NY, U. S.) **128**(6), 063102 (2020).
25. Z. A. Zaky, A. Panda, P. D. Pukhrambam, *et al.*, "The impact of magnetized cold plasma and its various properties in sensing applications," Sci. Rep. **12**(1), 3754 (2022).
26. A. D. Kaminker, G. G. Pavlov, and Y. A. Shibanov, "Radiation from a strongly-magnetized plasma: The case of predominant scattering," Astrophys. Space Sci. **86**(2), 249–297 (1982).
27. M. Wan, W. H. Matthaeus, H. Karimabadi, *et al.*, "Intermittent dissipation at kinetic scales in collisionless plasma turbulence," Phys. Rev. Lett. **109**(19), 195001 (2012).
28. J. B. Taylor and B. McNamara, "Plasma diffusion in two dimensions," Phys. Fluids **14**(7), 1492–1499 (1971).
29. L. Shiveshwari and P. Mahto, "Photonic band gap effect in one-dimensional plasma dielectric photonic crystals," Solid State Commun. **138**(3), 160–164 (2006).
30. B. Suthar and A. Bhargava, "Optical properties of plasma photonic crystals," Silicon **7**(4), 433–435 (2015).
31. Y. Ma, H. Zhang, T. Liu, *et al.*, "Properties of unidirectional absorption in one-dimensional plasma photonic crystals with ultra-wideband," Appl. Opt. **57**(28), 8119–8124 (2018).
32. Y. Liang, Z. Liu, L. Lin, *et al.*, "Transmission characteristics of electromagnetic waves in 2d tunable plasma photonic crystals," Appl. Opt. **60**(9), 2510–2516 (2021).
33. B. F. Wan, Y. Xu, Z. W. Zhou, *et al.*, "Theoretical investigation of a sensor based on one-dimensional photonic crystals to measure four physical quantities," IEEE Sensors J. **21**(3), 2846–2853 (2021).
34. A. H. M. Almawgani, D. N. Alhamss, S. A. Taya, *et al.*, "The properties of a tunable terahertz filter based on a photonic crystal with a magnetized plasma defect layer," Phys. Fluids **34**(8), 082020 (2022).
35. Z. A. Zaky, A. M. Ahmed, A. S. Shalaby, *et al.*, "Refractive index gas sensor based on the tamm state in a one-dimensional photonic crystal: Theoretical optimisation," Sci. Rep. **10**(1), 9736 (2020).
36. Y. Ma, H. Zhang, and C. Hu, "Tunable omnidirectional band gap and polarization splitting in one-dimensional magnetized plasma photonic crystals with a quasi-periodic topological structure," J. Opt. **22**(2), 025101 (2020).
37. Y. Wang, S. Liu, and S. Zhong, "Tunable multichannel terahertz filtering properties of dielectric defect layer in one-dimensional magnetized plasma photonic crystal," Opt. Commun. **473**, 125985 (2020).

Optics EXPRESS

38. Y. T. Fang and Y. C. Zhang, "Perfect nonreciprocal absorption based on metamaterial slab," Plasmonics **13**(2), 661–667 (2018).
39. R. Wangberg, J. Elser, E. E. Narimanov, *et al.*, "Nonmagnetic nanocomposites for optical and infrared negative-refractive-index media," J. Opt. Soc. Am. B **23**(3), 498–505 (2006).
40. Z. D. Wu, B. J. Xu, M. Y. Yan, *et al.*, "Broadband Microwave Absorber with a Double-Split Ring Structure," Plasmonics **15**(6), 1863–1867 (2020).